

K-Space-Aware Cross-Modality Score for Synthesized Neuroimage Quality Assessment

Jinbao Wang¹, Member, IEEE, Guoyang Xie¹, Yawen Huang¹, Jiayi Lyu, Feng Zheng, Member, IEEE, Yefeng Zheng, Fellow, IEEE, and Yaochu Jin, Fellow, IEEE

Abstract—The problem of how to assess cross-modality medical image synthesis has been largely unexplored. The most used measures like PSNR and SSIM focus on analyzing the structural features but neglect the crucial lesion location and fundamental k-space speciality of medical images. To overcome this problem, we propose a new metric K-CROSS to spur progress on this challenging problem. Specifically, K-CROSS uses a pre-trained multi-modality segmentation network to predict the lesion location, together with a tumor encoder for representing features, such as texture details and brightness intensities. To further reflect the frequency-specific information from the magnetic resonance imaging principles, both k-space features and vision features are obtained and employed in our comprehensive encoders with a frequency reconstruction penalty. The structure-shared encoders are designed and constrained with a similarity loss to capture the intrinsic common structural information for both modalities. As a consequence, the features learned from lesion regions, k-space, and anatomical structures are all captured, which serve as our quality evaluators. We evaluate the performance by constructing a large-scale cross-modality neuroimaging perceptual similarity (NIRPS) dataset with 6,000 radiologist judgments. Extensive experiments demonstrate that the proposed method outperforms other metrics, especially in comparison with the radiologists on NIRPS.

Index Terms—Medical image, quality assessment, synthesized neuroimages, k-space

I. INTRODUCTION

PSNR [15], SSIM [35], and MAE [7] are the most commonly used evaluation metrics in cross-modality magnetic resonance imaging (MRI) synthesis works. However, these metrics are inappropriate to a certain degree, considering that they are based on natural images and naturally ignore the inherent properties of MRI data. In general, the quality of neuroimage can be assessed by the content (*i.e.*, lesion region), frequency space, and structure details. Although MAE, PSNR

Jinbao Wang, Jiaqi Liu and Feng Zheng are with the Department of Computer Science and Engineering, Southern University of Science and Technology, Shenzhen 518055, China (e-mail: wangjb@ieee.org; liujq32021@mail.sustech.edu.cn; f.zheng@ieee.org)

Guoyang Xie is with the Department of Computer Science and Engineering, Southern University of Science and Technology, Shenzhen 518055, China and is also with the Department of Computer Science, University of Surrey, Guildford GU2 7YX, United Kingdom (e-mail: guoyang.xie@surrey.ac.uk)

Yawen Huang and Yefeng Zheng are with Tencent Jarvis Lab, Shenzhen 518040, China (e-mail: bear_huang@126.com; yefengzheng@tencent.com).

Jiayi Lyu is with the School of Engineering Science, University of Chinese Academy of Sciences, Beijing, China (e-mail: lyujiayi21@mails.ucas.ac.cn)

Yaochu Jin is with the Faculty of Technology, Bielefeld University, 33619 Bielefeld, Germany and also with the Department of Computer Science and Engineering, University of Surrey, Guildford GU2 7YX, United Kingdom (e-mail: yaochu.jin@uni-bielefeld.de)

¹Contributed Equally.

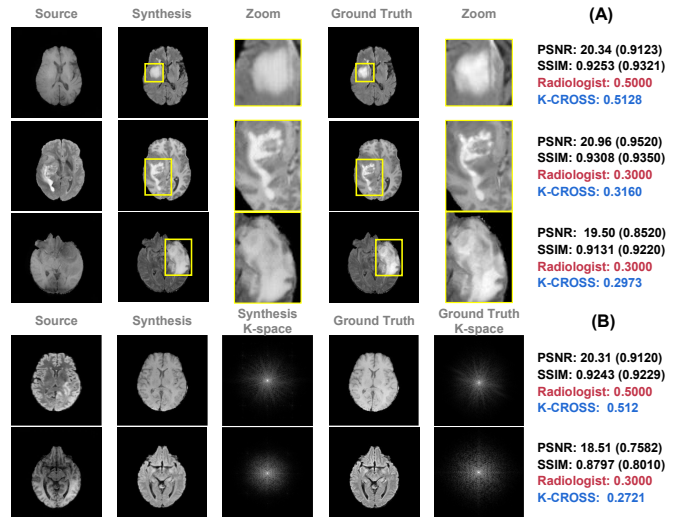


Fig. 1. K-CROSS vs. PSNR vs. SSIM. The first and second columns on the left represent the source and synthesized target modality data, respectively. The zoom indicates the modality-specific tumor region, which is provided by the pre-trained multi-modality neuroimage segmentation network. The numbers on the right represent PSNR, SSIM, radiologist score, and our K-CROSS value. PSNR, SSIM, and K-CROSS are rescaled (to 1.0000) for comparison with the radiologist's score. In terms of lesion region and k-space measurement, K-CROSS is more compatible with the radiologist's score than PSNR and SSIM.

and SSIM are effective in assessing image quality, they are ineffective as a neuroimage metric, because they only focus on the structural details in the pixel space. Therefore, it is important to find a new way to measure how good the cross-modality neuroimage synthesis is.

Empirically, the content details of neuroimages, particularly the texture and brightness, are disregarded by either PSNR or SSIM. Instead, radiologists pay more attention to the lesion regions, since the usefulness of analyzing pathology and human cognitive functions. The purpose of K-CROSS is to fully reflect the lesion region by introducing a cross-modality neuroimage segmentation network which has already been trained to precisely forecast the tumor location. The prediction mask (*i.e.*, tumor region) is fed into the proposed tumor encoder to extract features. The proposed tumor loss function improves the extracted feature to capture more essential texture details and brightness information. In Fig. 1 (A), we can observe that the content of the synthesis neuroimage does not align with the target modality neuroimage. Though PSNR and SSIM scores are the highest for the synthesized ones, they only evaluate the structure details without taking the

content into account. By contrast, K-CROSS is reliable in exploring neuroimaging perceptual similarity (NIRPS) for the synthesized results.

Besides, PSNR and SSIM are unable to account for differences in the k-space between the synthesized images and the target modality data, whereas K-CROSS can. The fundamental difference between MRI and natural images, as seen from the standpoint of imaging principles, is the basis of MR image reconstruction. The Fourier transformation, often known as the "k-space" in MRI, is a mathematical concept that calculates various frequencies mixed into the received signal of all spins. It forms the basis for all image reconstruction in MRI. Therefore, we believe that the proposed metric can estimate the distance between MRIs in both k-space and pixel space. In k-space, the sophisticated K-CROSS encoder can capture the invariant modal-specific feature, where the frequency loss can be used to further enhance the complicated encoder. When a k-space shift occurs, as seen at the bottom of Fig. 1 (B), K-CROSS is more stable in accordance with the radiologist's score, which is able to measure the gap in k-space between the synthesized neuroimage and the corresponding ground truth.

To constrain the structural features that are extracted by the shared structure encoder from both the source modality and the target modality, we set up a cross-modality similarity loss function, as the entire structure information between the source and the target modality neuroimaging data is very similar. PSNR and SSIM, on the other hand, only assess the input image, which limits their capacity to recognize the structural details that the source modality and the target modality share.

Our contributions can be summarized as follows:

- We propose a new metric, called K-CROSS, to evaluate the quality of the synthetic data based on all the structural information, k-space feature shift, and lesion area. This multidimensional quantification indication enables K-CROSS to achieve more precise results than other metrics that only consider natural images.
- To properly verify the effectiveness of our K-CROSS, we construct a large-scale and multi-modal neuroimaging perceptual similarity (NIRPS) dataset, which includes 6,000 assessments from radiologists.
- K-CROSS achieves highly competitive results based on the judgments from radiologists on NIRPS, which can be treated as a general evaluation metric for various purposes of medical image synthesis.

The rest of this paper is organized as follows: Section II presents a literature review on image quality assessment and GAN-based assessment methods. Section III explains the proposed algorithm K-CROSS in detail. In addition, a large-scale multi-modal neuroimaging perceptual similarity (NIRPS) dataset is constructed in Section IV. Section V presents comprehensive experimental evaluations while Section V draws the conclusion and limitation of the current work.

II. RELATED WORK

A. Image Quality Assessment

Image quality assessment (IQA) can be divided into two categories. One is fully referenced IQA, and the other is

non-referenced IQA [24], [25], [5], [33]. IQA with all references refers to estimating the quality of natural images with references: SSIM [35], MS-SSIM [36] and FSIM [40], focus more on image structure specifics. Specifically, FSIM builds up a novel feature similarity index according to the phase congruence and image gradient magnitude, while PSNR focuses on edge estimation for the synthesized images. Most of them [20], [26], [32], [42] use low-level features for evaluation. LPIPS [41] is the first work that uses a high-level feature for fully referenced IQA in light of the popularity of deep learning. Estimating the synthesized image quality without a reference (ground truth) is known as non-referenced IQA [24], [25], [5], [33]. RankIQA [22] is the mainstream for non-referenced IQA. Considering the limited size of IQA, Liu *et al.* propose a Siamese network to rank images and their distorted ones. The Siamese network's knowledge (ranking result) can be transferred to a conventional neural network, whose function is to assess the quality of a single image. Since K-CROSS requires a reference image for evaluation, it belongs to a fully referenced IQA. However, few public data in the medical imaging community could be used to train for the learning-based fully referenced IQA methods. The NIRPS dataset, the first extensive neuroimaging perceptual similarity dataset with radiologists' labels is constructed. As for fully referenced IQA methods, K-CROSS is, therefore, able to use the supervised training methods.

B. GAN Assessment

The existing sample-based methods [38] have been proposed to access GAN performance, like Kernel MMD [12], Inception Score [27], Mode Score [8] and FID [13]. The classical approach is to compare the log-likelihood of generative models. But this approach cannot accurately indicate the quality of synthesized image. In other words, a model can achieve high likelihood, but low image quality, and conversely, low image quality, and conversely. As for Inception score [27], it computes the KL divergence between the conditional class distribution and the marginal class distribution over the generated data. However, IS does not capture intra-class diversity, which is insensitive to the prior distribution over labels. Among them, the most popular metric is FID. Heusel *et al.* [13] use InceptionV3 [31] to extract the features from the real and synthetic neuroimaging data, and then compute the differences in the features between them. However, the majority of them are created in the pixel space and ignore the lesion region and k-space, which are the fundamental elements of MR image properties. In this regard, K-CROSS considers the underlying MR imaging principle as well as the difference between the neuroimages of the source and target modality.

III. PROPOSED METHOD

A. Preliminary

1) *K-Space Representations*: The spatial frequencies of an MR picture are represented in k-space by a matrix of numbers. Despite MR images and k-space having the identical dimension, in practice, each point (k_x, k_y) in k-space represents the spatial frequency and phase information about each pixel in

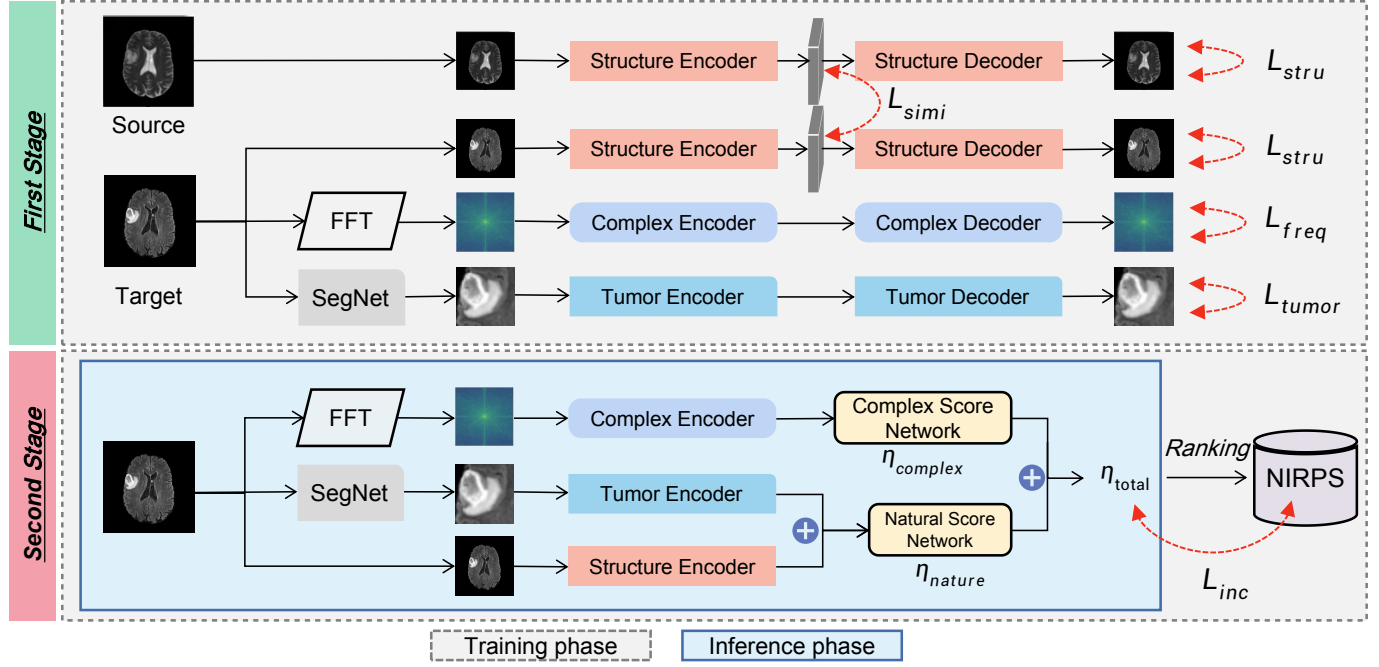


Fig. 2. Flowchart of our proposed K-CROSS. **First stage input:** For reference neuroimage (source modality) and its query neuroimage (the target modality), the private portion is indicated by a blue box. The neuroimage's structural feature is captured by the structure encoder. The reconstruction specifics are evaluated using L_{stru} . With a similarity loss L_{simi} , the presentation of the shared structure is maintained. The k-space feature to a modality is captured by Complex U-Net and optimized by L_{freq} . SegNet gets the mask of the tumor region from neuroimages that are specific to a given modality. The parameters of the off-the-shelf SegNet are not updated during the training phase, such as nnUNet [16], TransUNet [9], and SwinUNet [6]. The tumor encoder learns how to represent the tumor mask region, particularly texture details and the level of brightness. The quality of the SegNet-reconstructed tumor region is constrained using the loss L_{tumor} . **First stage output:** The private tumor encoder, the private complex encoder and the shared structure encoder for both modalities. **Second stage input:** The input are the query modality neuroimage and the modality-specific tumor encoder, complex encoder and the shared structure encoder from the first stage. The two main components of K-CROSS are $\eta_{complex}$ and η_{nature} . The complex score network yields $\eta_{complex}$, whereas the natural score network yields η_{nature} . The output of the tumor encoder and the structure encoder are combined as the input of the natural score network. The average score for $\eta_{complex}$ and η_{nature} is η_{total} . For η_{total} , K-CROSS uses a straightforward regression model during the training phase, with labels taken from the NIPRS dataset. **Inference:** The input are the query modality neuroimage and the modality-specific tumor encoder, complex encoder and the shared structure encoder from the first stage. The output score is η_{total} .

the MR image rather than corresponding to a specific pixel value. By contrast, every pixel in the MR image maps to a point in k-space. As a result, we transform MRI into k-space using the 2D discrete Fourier transform:

$$F(u, v) = \sum_{x=0}^{M-1} \sum_{y=0}^{N-1} f(x, y) e^{-i2\pi(\frac{ux}{M} + \frac{vy}{N})}, \quad (1)$$

where the MR image size is $M \times N$, (x, y) is the MRI's pixel coordinate, (u, v) is its spatial coordinate in k-space, $F(u, v)$ is its complex frequency value, and e and i stand for the Euler's number and the imaginary unit, respectively. We concentrate on the real and imaginary components of $F(u, v)$. According to (1), we rewrite $F(u, v)$ as follows:

$$F(u, v) = R(u, v) + I(u, v)i = a + bi, \quad (2)$$

where the imaginary and real parts of $F(u, v)$ are $I(u, v)$ and $R(u, v) = a$, respectively. Furthermore, we introduce two key k-space concepts. Here, the amplitude can be defined as:

$$|F(u, v)| = \sqrt{R(u, v)^2 + I(u, v)^2} = \sqrt{a^2 + b^2}. \quad (3)$$

The amplitude is a measure of how strongly a 2D wave reacts to an MR image. We typically visualize k-space using the

amplitude.

$$\angle F(u, v) = \arctan \left(\frac{I(u, v)}{R(u, v)} \right) = \arctan \left(\frac{b}{a} \right). \quad (4)$$

The peak shift distance between two 2D sinusoidal waves of the same frequency is referred to as a phase. The phase is the second concept, which is defined in (4).

2) *Complex Convolution*: The complex-valued convolution [34] is different from the real-valued convolution. Given a complex-valued convolution filter $\mathbf{W} = \mathbf{A} + i\mathbf{B}$ with real-valued matrices \mathbf{A} and \mathbf{B} . The operation is expressed as follows:

$$\mathbf{W} * \mathbf{h} = (\mathbf{A} * \mathbf{x} - \mathbf{B} * \mathbf{y}) + i(\mathbf{B} * \mathbf{x} + \mathbf{A} * \mathbf{y}). \quad (5)$$

The visualization can be found in Fig. 4.

3) *Complex Leaky RELU*: It applies separate Leaky RELUs [23] on both the real part $\mathbf{R}(z)$ and the imaginary part $\mathbf{Im}(z)$ of a complex-valued, which is defined as:

$$\mathbb{C}\text{LeakyReLU} = \text{LReLU}(\mathbf{R}(z)) + i * \text{LReLU}(\mathbf{Im}(z)), \quad (6)$$

4) *Complex RELU*: It applies separate RELUs [1] on both the real part $\mathbf{R}(z)$ and the imaginary part $\mathbf{Im}(z)$ of a complex-valued, which is defined as:

$$\mathbb{C}\text{RELU} = \text{RELU}(\mathbf{R}(z)) + i * \text{RELU}(\mathbf{Im}(z)). \quad (7)$$

The visualization is given in Fig. 5.

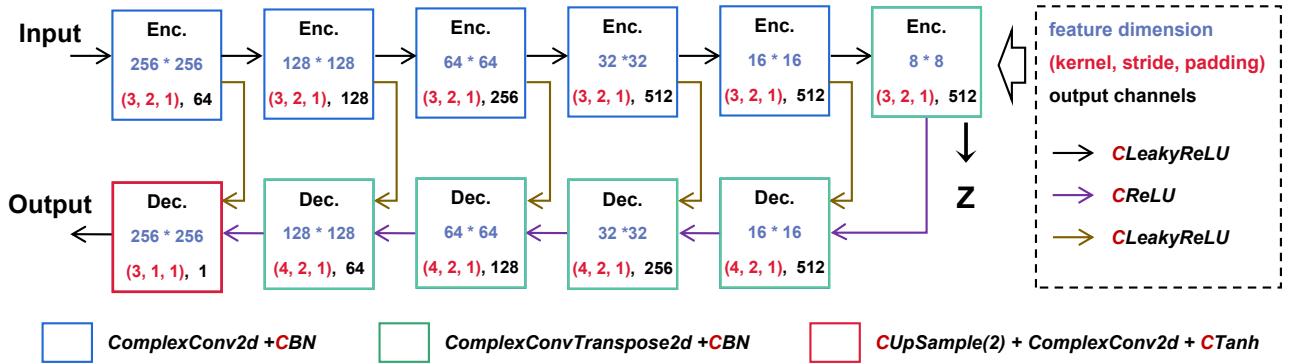


Fig. 3. The architecture of complex encoder and decoder. The encoder consists of Complex Conv2d in Section III-A2 and Complex BatchNorm in Section III-A6. The decoder contains ComplexConvTranspose2d and Complex BatchNorm. The ComplexConvTranspose2d is similar to ComplexConv2d except for the convolution operator. The middle part includes Complex Upsample in Section III-A7, Complex Tanh in Section III-A5 and Complex Conv2d.

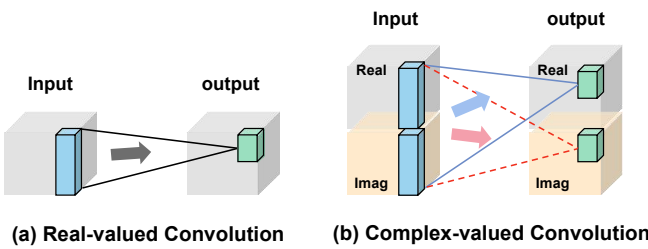


Fig. 4. Illustration of complex convolution.

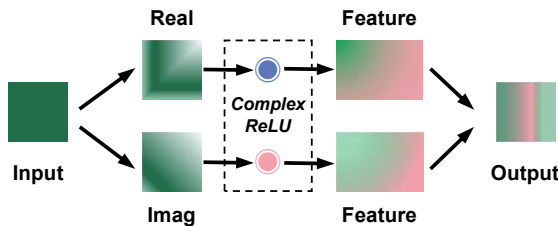


Fig. 5. Illustration of complex operator.

5) *Complex Tanh*: Complex Tanh applies separate tanh activation [18] on both the real part $\mathbf{R}(z)$ and imaginary part $\mathbf{Im}(z)$ of a complex-valued, which is defined as:

$$\mathbf{CTanh} = \mathbf{Tanh}(\mathbf{R}(z)) + i * \mathbf{Tanh}(\mathbf{Im}(z)). \quad (8)$$

6) *Complex BatchNorm*: As described in Cogswell *et al.* [10], complex-valued batch normalization could be separately applied into the imaginary part and real part, which could reduce the risk of over-fitting. The detail operation is defined as:

$$\mathbf{CBN} = \mathbf{BN}(\mathbf{R}(z)) + i * \mathbf{BN}(\mathbf{Im}(z)). \quad (9)$$

7) *Complex Upsample*: complex-valued upsample algorithm is able to be separately applied to the real part and imaginary part, which is defined as:

$$\mathbf{CUpsample} = \mathbf{Upsample}(\mathbf{R}(z)) + i * \mathbf{Upsample}(\mathbf{Im}(z)). \quad (10)$$

B. Architecture

1) *Complex Branch*: A more refined U-Net architecture implemented in k-space makes up the proposed complex encoder. Specifically, each downsampling block in the encoding stage includes complex convolution \mathbf{CBN} and $\mathbf{CLeakyReLU}$. The complex convolution is replaced with the complex transposed convolution for up-sampling during the decoding phase. There is a complex transposed convolution, \mathbf{CBN} , and \mathbf{CRELU} in each upsampling block. We apply $\mathbf{CUpsample}$, complex convolution and \mathbf{CTanh} to reconstruct the images in the final layer of the decoding stage. Fig. 3 shows the complex branch architecture in detail.

2) *Tumor and Structure Branch*: As a cross-modality segmentation neural network, the well-trained nnU-Net [16] is used in K-CROSS, with the weights being adjusted in the second stage of training. The modality-specific tumor encoder and decoder are private because the tumor information (the texture details and brightness) from the source modality and the target modality differ. With the exception of the operators using the normal convolution, batch norm, and Leaky RELU, the architecture details of the tumor encoder-decoder and the structure encoder-decoder are similar to those of Fig. 3.

3) *Score Network and Quality Prediction Regressor*: We construct a two-layer MLP for quality prediction, considering that the regressor simply maps the output vectors of the triple-path decoder to labeled quality scores. The network is made up of two fully connected layers with 512-256 and 256-1 channels. The complex score network is composed of two complex fully interconnected layers. Its structure is similar to that shown in Fig. 5. However, the operator of the complex score network substitutes MLP layers for \mathbf{CRELU} . The natural score network has two fully connected layers as well. The channels of the complex score network and the natural score network are 512-256 and 256-1, respectively. The regressor is trained by using the L_1 loss function.

C. Loss Function

1) *Frequency Loss*: Directly measuring the distance between two complex vectors is very difficult. Alternatively, recent works are more concerned with the image amplitude.

We discover that without the phase information from Fig. 6, which is impossible to reconstruct the entire neuroimage.

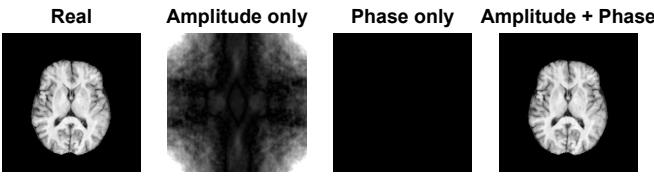


Fig. 6. Illustration of the k-space amplitude and phase of images. When only the amplitude or phase is given, the reconstructed image will lose the information of the real image.

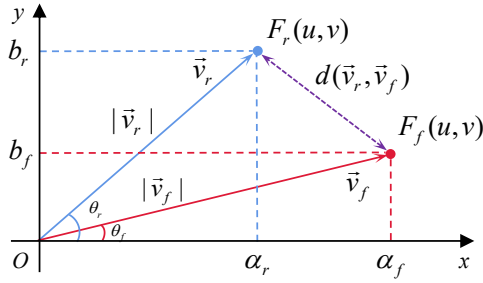


Fig. 7. Frequency loss: the distance between \vec{v}_r and \vec{v}_f corresponds to the distance between F_r and F_f .

Our solution is based on the focal frequency loss [17], as shown in Fig. 7. The hidden k-space of real MRI is $F_r(u, v) = a_r + b_r i$, and the corresponding k-space of synthesis MRI is $F_f(u, v) = a_f + b_f i$. To calculate their distance, we map F_r and F_f into the Euclidean space as \vec{v}_r and \vec{v}_f . Specifically, the lengths of \vec{v}_r and \vec{v}_f are the amplitudes of F_r and F_f , respectively. And the angles θ_r and θ_f correspond to the phases of F_r and F_f , respectively. As a result, the distance between F_r and F_f can be converted to the distance between \vec{v}_r and \vec{v}_f (termed as $d(\vec{v}_r, \vec{v}_f)$), which is defined as follows:

$$d(F_r, F_f) = d(\vec{v}_r, \vec{v}_f) = \|\vec{v}_r - \vec{v}_f\|^2. \quad (11)$$

The complex feature maps are extracted from each layer l of the encoder in the complex U-Net. Each pixel of the complex feature maps for each layer is denoted as $m^l \in \mathbb{R}^{H_l \times W_l \times C_l}$. Finally, we compute spatial and channel averages. As a result, the frequency loss for a complex U-Net is defined as follows:

$$\mathcal{L}_{freq}(m_r^l, m_f^l) = \sum_l \frac{1}{H_l W_l} \sum_{h,w} \|\vec{v}_r - \vec{v}_f\|^2. \quad (12)$$

2) *Similarity Loss*: For the similarity loss \mathcal{L}_{simi} , K-CROSS uses the maximum mean discrepancy (MMD) loss [30] to measure it. That is, K-CROSS computes the squared population MMD between shared structure encoding of the source

modality h_c^s and the target modality h_t^s using a biased statistic. We express this as:

$$\begin{aligned} \mathcal{L}_{simi} = & \frac{1}{(N^s)^2} \sum_{i,j=0}^{N^s} \kappa(h_{c_i}^s, h_{c_j}^s) - \frac{2}{N^s N^t} \sum_{i,j=0}^{N^s, N^t} \kappa(h_{c_i}^s, h_{c_j}^s) \\ & + \frac{1}{(N^t)^2} \sum_{i,j=0}^{N^t} \kappa(h_{c_i}^s, h_{c_j}^s), \end{aligned} \quad (13)$$

where κ is a linear combination of multiple RBF kernels: $\kappa(x_i, x_j) = \sum_n \eta_n \exp \left\{ -\frac{1}{2\sigma} \|x_i - x_j\|^2 \right\}$, where σ_n is the standard deviation and η_n is the weight for n -th RBF kernel. The similarity loss function encourages the shared structure encoder to learn the invariant structure feature irrespective of the modality.

3) *Tumor Loss*: The tumor loss function consists of a Laplacian loss function \mathcal{L}_{lap} and the LPIPS loss function \mathcal{L}_{lapis} [41]. The Laplacian loss function is defined as :

$$\mathcal{L}_{lap} = \mathbb{E} \|L(x) - L(\hat{x})\|_2^2. \quad (14)$$

The LPIPS loss function is defined as:

$$\mathcal{L}_{lapis} = \sum_k \tau^k (\phi^k(x) - \phi^k(\hat{x})). \quad (15)$$

So the tumor loss is described below:

$$\mathcal{L}_{tumor} = \lambda_{lap} \mathcal{L}_{lap} + \lambda_{lapis} \mathcal{L}_{lapis}. \quad (16)$$

In (15), $\phi(\cdot)$ represents the feature extractor and $\tau(\cdot)$ computes the feature score from the k -th layer of the backbone architecture. As a result, the LPIPS value is the average score of all backbone layers. To compute the LPIPS loss, we used a well-trained VGG [30] network. The Laplacian loss is used to identify the tumor region's high-frequency component. Due to LPIPS loss, the real tumor region and the reconstructed tumor region are more similar, which is more consistent with the radiologist's judgment.

4) *Structure Loss*: We employ L_1 loss function to extract meaningful semantic structure features, where the structure loss function is defined as:

$$\mathcal{L}_{stru} = \|x - \hat{x}\|_1. \quad (17)$$

5) *Inconsistency Loss*: We adopt the MSE loss function to optimize the weights of complex score network n_c and natural score network n_{nat} , where the inconsistency loss is defined as:

$$\mathcal{L}_{inc} = \|\eta_{total} - \eta_{ra}\|_1, \quad (18)$$

where the score of K-CROSS η_{total} is aligned with the scale of the radiologist's rating score η_{ra} via our proposed ranking algorithm. The details of the ranking algorithm can be found in Algorithm 4.

6) *Total Loss*: For the first stage, the loss function is described below:

$$\mathcal{L}_{first} = \lambda_1 \mathcal{L}_{tumor} + \lambda_2 \mathcal{L}_{stru} + \lambda_3 \mathcal{L}_{freq} + \lambda_4 \mathcal{L}_{simi}. \quad (19)$$

In the second stage, we optimize the parameters of the complex score network and the natural score network via

$$\mathcal{L}_{second} = \mathcal{L}_{inc}. \quad (20)$$

In this work, all weights of λ are set to 1.

TABLE I
DESCRIPTION FOR NOTATIONS USED IN OUR ALGORITHMS.

Notation	Description
s	Source neuroimage
t	Paired target neuroimage
\hat{t}	Synthesized target modality neuroimage
Ω_{ref}	Reference images
Ω_{syn}	Synthesised images
φ_E	Tumor encoder
φ_D	Source tumor decoder
ψ_E	Source complex encoder
ψ_D	Complex decoder
ξ_E	Shared structure encoder
ξ_D	Shared structure decoder
ν	Segmentation network
FT	Fourier transform
l	Lesion mask
ζ	K-space function
z	Structural feature
θ_X^n	The parameters of X trained in stage n
n_c	Complex score network
n_{nat}	Natural score network
η_{ra}	Radiologist rating score
η_{total}	K-CROSS score

Algorithm 1: K-CROSS training stage 1

Input : $s, t, \varphi_E, \varphi_D, \psi_E, \psi_D, \xi_E, \xi_D, \nu, FT, l, \zeta$, and z
Output: $\theta_{\varphi_E}^1, \theta_{\varphi_D}^1, \theta_{\psi_E}^1, \theta_{\psi_D}^1, \theta_{\xi_E}^1$, and $\theta_{\xi_D}^1$

- 1 $l_t \leftarrow \nu(t)$ // generate lesion mask of target neuroimage
- 2 $\zeta_t \leftarrow FT(t)$ // convert k-space of target neuroimage
- 3 $z_s \leftarrow \xi_E(s)$ // compute structure feature of source neuroimage
- 4 $z_t \leftarrow \xi_E(t)$ // convert structure feature of target neuroimage
- 5 **while** not converged **do**
- 6 Update $\theta_{\psi_E}^1$ and $\theta_{\psi_D}^1$ with κ_t , \mathcal{L}_{freq} in (12)
- 7 Update $\theta_{\varphi_E}^1$ and $\theta_{\varphi_D}^1$ with l_t , \mathcal{L}_{tumor} in (16)
- 8 Update $\theta_{\xi_E}^1$ and $\theta_{\xi_D}^1$ with $z_s, z_t, \mathcal{L}_{simi}$ in (13) and \mathcal{L}_{stru} in (17)
- 9 **end while**

D. Algorithms

The two stages of training K-CROSS are depicted in Fig 2. The details of two-stage training algorithms and the inference algorithm are described in Algorithm 1, Algorithm 2 and Algorithm 3, respectively. For clarity, Table I provides notation descriptions that occurred in our algorithms.

IV. NIRPS DATASET AND RADIOLOGIST SCORE

To comprehensively evaluate the synthesis performance, we construct a large-scale multi-modal neuroimaging perceptual similarity (NIRPS) dataset with 6,000 radiologist judgments. NIRPS dataset is composed of three subsets generated by CycleGAN [44], MUNIT [14] and UNIT [21]. Each set contains 800 images generated by IXI and 1,200 images generated by BraTS. The IXI dataset includes two modalities, PD and T2, while the BraTS dataset includes three modalities, T1, T2, and FLAIR. In both the IXI and BraTS datasets, we randomly select 10 slices for training and collect the training results after each epoch of the model trained over 40 epochs.

Algorithm 2: K-CROSS training stage 2

Input : $\hat{t}, \varphi_E, \theta_{\varphi_E}^1, \psi_E, \theta_{\psi_E}^1, \xi_E, \theta_{\xi_E}^1, n_c$, and n_{nat}
Output: θ_{n_c} , $\theta_{n_{nat}}$

- 1 $\zeta_{\hat{t}} \leftarrow FT(\hat{t})$ // convert k-space of synthesis target neuroimage
- 2 $l_{\hat{t}} \leftarrow \nu(\hat{t})$ // generate lesion mask of synthesis target neuroimage
- 3 $f_{complex} \leftarrow \psi_E(\zeta_{\hat{t}})$ // compute the complex feature
- 4 $f_{tumor} \leftarrow \varphi_E(l_{\hat{t}})$ // compute the tumor feature
- 5 $f_{stru} \leftarrow \xi_E(\hat{t})$ // compute the structure feature
- 6 $\eta_{complex} \leftarrow n_c(f_{complex})$ // compute the complex score
- 7 $\eta_{nat} \leftarrow n_{nat}(f_{tumor} + f_{stru})$ // compute the nature score
- 8 $\eta_{total} \leftarrow \eta_{nat} + \eta_{complex}$
- 9 Ranking all η_{total} and get in line with η_{ra}
- 10 **while** not converged **do**
- 11 Update θ_{n_c} and $\theta_{n_{nat}}$ with η_{total} , η_{ra} and \mathcal{L}_{inc} in (18)
- 12 **end while**

Algorithm 3: K-CROSS inference

Input : $\hat{t}, \varphi_E, \theta_{\varphi_E}^1, \psi_E, \theta_{\psi_E}^1, \xi_E, \theta_{\xi_E}^1, n_c, \theta_{n_c}, n_{nat}, \theta_{n_{nat}}, FT$, and ν
Output: η_{total}

- 1 $\zeta_{\hat{t}} \leftarrow FT(\hat{t})$ // convert k-space of synthesis target neuroimage
- 2 $l_{\hat{t}} \leftarrow \nu(\hat{t})$ // generate lesion mask of synthesis target neuroimage
- 3 $f_{complex} \leftarrow \psi_E(\zeta_{\hat{t}})$ // compute the complex feature
- 4 $f_{stru} \leftarrow \xi_E(\hat{t})$ // compute the structure feature
- 5 $\eta_{complex} \leftarrow n_c(f_{complex})$ // compute the complex score
- 6 **if** $\hat{t} \in \text{healthy person}$ **then**
- 7 $\eta_{nat} \leftarrow f_{stru}$
- 8 **else**
- 9 $l_{\hat{t}} \leftarrow \nu(\hat{t})$ // generate lesion mask of synthesis target neuroimage
- 10 $f_{tumor} \leftarrow \varphi_E(l_{\hat{t}})$ // compute the tumor feature
- 11 $\eta_{nat} \leftarrow n_{nat}(f_{tumor} + f_{stru})$
- 12 **end if**
- 13 $\eta_{total} \leftarrow \eta_{nat} + \eta_{complex}$
- 14 Ranking all η_{total} and get in line with η_{ra}

IXI [2] collects nearly 600 MR images from normal and healthy subjects at three hospitals. The MR image acquisition protocol for each subject includes T1, T2, PD-weighted images (PD), MRA images, and Diffusion-weighted images. In this paper, we only use T1 (581 cases), T2 (578 cases) and PD (578 cases) data to conduct our experiments, and select the paired data with the same ID from the three modes. The image has a non-uniform length on the z-axis with the size of 256 on the x-axis and y-axis. The IXI dataset is not divided into a training set and a test set. Therefore, we randomly split the whole data as the training set (80%) and the test set (20%).

BraTS2021 [29], [3] is designed for brain disease analysis and diagnosis. The dataset of multi-institutional and pre-operative MRI sequences is made publicly available, and it includes both training data (1251 cases) and validation data (219 cases). Each 3D volume is $155 \times 240 \times 240$ in size and is imaged by four sequences: T1, T2, T1ce, and FLAIR.

Training Data Processing To ensure data validity and diversity, we remove their skulls for each slice, by splitting the three-dimensional volume and choosing slices ranging from

Algorithm 4: Calculate inconsistency by ranking

```

1 Input: reference images  $\Omega_{ref}$ , synthesised images  $\Omega_{syn}$ 
2 Initialize: start = 0, pairwise  $\leftarrow \phi$ , uniform_result  $\leftarrow \phi$ 
3 // count elements in levels
4 recounted = Collection.Counter( $\Omega_{ref}$ )
5 // obtain the sorted level of reference images
6 level = sorted(recounted)
7 // obtain the indices of synthesised images
8 index = numpy.argsort( $\Omega_{syn}$ )
9 // obtain the number of images  $\Omega_{ref}$  in each level
10 for  $l$  in level do
11   end = start + recounted[ $l$ ]
12   pairwise.append([start, end])
13   start = end
14 end for
15 // obtain uniformed results  $\Omega_{syn}$ 
16 for  $v$  in index do
17   for  $i, p$  in enumerate(pairwise) do
18     if  $v$  in range( $p[0], p[1]$ ) then
19       uniform_result.append( $i / \text{len}(\text{level})$ )
20       break
21     end if
22   end for
23 end for
24 // calculate consistency
25 Return:  $\|\Omega_{ref} - \Omega_{syn}\|_1 \cdot \text{mean}()$ 

```

50 to 80 on the z-axis. All images are cropped to 256 pixels in size. During the training stage, we choose a total of 10k images from the IXI and BraTS2021 datasets.

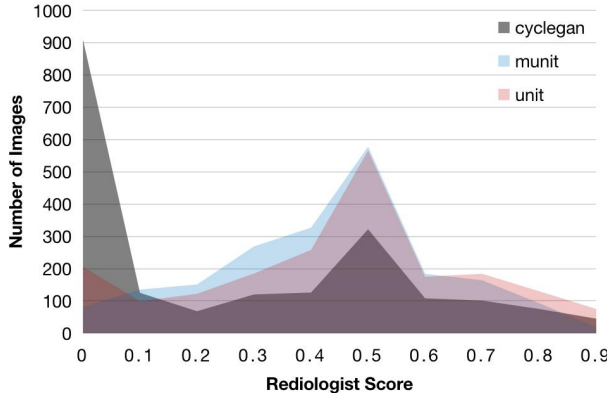


Fig. 8. Statistical results of NIRPS.

1) Radiologist Score: The NIRPS dataset contains radiologist scores (RS) resulting from manual annotation for each image. It is worth noting that the radiologist score RS includes 10 levels, i.e., $RS \in [0, 0.1, 0.2, \dots, 0.9]$. The higher RS value indicates better-synthesized neuroimage quality. The radiologists give scores in accordance with the level of diagnosis and therapy by using the synthesized neuroimage. Fig. 8 gives the distribution result of RS . We can see that synthesized performance varies among the three models and the average RS is in the middle.

2) How Radiologists Assess?: We prepare the real paired modalities neuroimage dataset M in advance. M consists of source modalities M_s and target modalities M_t . We generate the synthesized target modality neuroimages \hat{M}_t via feeding

TABLE II

PERFORMANCE COMPARISON OF VARIOUS IQA METHODS ON NIRPS. NIRPS INCLUDES THREE SUBSETS GENERATED BY CYCLEGAN, MUNIT, AND UNIT. SPECIFICALLY, EACH SET CONSISTS OF 800 IMAGES FOR IXI AND 1,200 IMAGES FOR BRATS. HERE, IXI AND BRATS TRAINING SETS ARE USED TO TRAIN OUR MODEL. THE INCONSISTENCY IS COMPUTED, WHERE \downarrow IS BETTER. THE BEST RESULT IS HIGHLIGHTED IN RED.

Metric	CycleGAN		MUNIT		UNIT	
	IXI	BraTS	IXI	BraTS	IXI	BraTS
MAE [7]	0.3127	0.3335	0.1807	0.2368	0.2462	0.2462
PSNR [15]	0.3387	0.2060	0.1832	0.2515	0.2387	0.2585
SSIM [35]	0.3333	0.1998	0.1957	0.2437	0.2523	0.2645
MS-SSIM [36]	0.3245	0.1973	0.1934	0.2425	0.2487	0.2521
NLPD [19]	0.3128	0.1961	0.1921	0.2408	0.2466	0.2445
GMSD [39]	0.3069	0.1952	0.1910	0.2395	0.2421	0.2432
DeepIQA [4]	0.3052	0.1943	0.1827	0.2380	0.2402	0.2410
LPIP [41]	0.3023	0.1921	0.1786	0.2285	0.2398	0.2327
DIST [11]	0.3012	0.1901	0.1725	0.2291	0.2387	0.2230
K-CROSS	0.2878	0.1851	0.1650	0.2246	0.2123	0.2147

M_s into the generative model, i.e., CycleGAN, MUNIT and UNIT in NIPRS. Then radiologist gives the score for \hat{M}_t according to the comparison with M_t . For instance, we have paired ground-truth modality datasets, T1 and T2. As shown in Fig. 9, we synthesized the fake T2 by feeding T1 into the MUNIT model. The radiologists make direct comparisons between fake T2 and real T2 and give their score for the synthesized quality of T2.

3) How Radiologists Combine Their Evaluations?: We hire 10 radiologists to evaluate the quality of each synthesized neuroimage. We remove the highest score and the lowest score from all radiologists. Then the final score is averaged by the rest score from 8 radiologists.



Fig. 9. Labelling tools in our artificial score system. The first column denotes the ground-truth T2 neuroimage. The second column denotes the synthesized T2 neuroimage. The third column is the error map between the ground truth neuroimage and its synthesized one.

V. EXPERIMENT AND ABLATION STUDY

A. K-CROSS vs Other Metrics

Table II illustrates the inconsistency between metrics and human evaluations of several datasets and generative models, with the highest performance shown in red. The calculation method for inconsistency value is given in Algorithm 4. We evaluate K-CROSS on datasets created by CycleGAN, MUNIT, and UNIT. The first column indicates various IQA methods. The second column indicates which datasets were used to train the K-CROSS model, including IXI or BraTS.

From Table II, our proposed K-CROSS is more compatible with the assessments of radiologists. Note that the IXI dataset is a healthy person dataset. There is no lesion for each neuroimage. So K-CROSS only use the tumor branch and complex branch to assess the quality of neuroimage. The details are described in Section V-C.

B. K-Space Importance

Table III records the ablation study of individual branches (the complex branch, tumor branch and structure branch) on various datasets. For instance, when we conduct the ablation study of the complex branch, K-CROSS remove the tumor branch and structure branch in the inference phase. In other words, K-CROSS only obtain $\eta_{complex}$ score. It applies the same setting for the other branches. It can be clearly observed that the complex branch obtain the highest score among the three branches. It strongly indicates the importance of k-space, which reflects the inherent properties of magnetic resonance imaging principles. The second best is the tumor branch. It also verifies the effectiveness of the tumor branch for the lesion disease dataset.

TABLE III

EFFECT OF K-SPACE IMPORTANCE (COMPLEX BRANCH) AND TUMOR BRANCH. THE INCONSISTENCY IS COMPUTED, WHERE \downarrow IS BETTER. THE BEST RESULT IS IN RED AND THE SECOND BEST RESULT IS IN BLUE.

Model	Structure Branch	Complex Branch	Tumor Branch	All
	$\mathcal{L}_{stru} + \mathcal{L}_{simi}$	\mathcal{L}_{freq}	\mathcal{L}_{tumor}	
<i>BraTS TI \leftrightarrow FLAIR</i>				
CycleGAN	0.1970	0.1911	0.1920	0.1880
MUNIT	0.2348	0.2273	0.2338	0.2250
UNIT	0.2333	0.2210	0.2248	0.2102
<i>BraTS T2 \leftrightarrow FLAIR</i>				
CycleGAN	0.1983	0.1889	0.1953	0.1853
MUNIT	0.2365	0.2272	0.2348	0.2250
UNIT	0.2305	0.2250	0.2297	0.2155
<i>BraTS TI \leftrightarrow T2</i>				
CycleGAN	0.1839	0.1836	0.1953	0.1819
MUNIT	0.2332	0.2258	0.2308	0.2239
UNIT	0.2595	0.2290	0.2298	0.2183

C. Metrics for Healthy Person

Table IV shows K-CROSS performance that surpasses the mainstream IQA methods on the IXI healthy-person dataset. As for assessing the synthesised neuroimage of healthy persons, K-CROSS removes the tumor branch in the inference phase. Because there are no lesions on healthy person datasets. It means that K-CROSS only combines $\eta_{complex}$ and the score of the structure encoder as the final score. From Table IV, it can be obviously observed that K-CROSS complex branch score $\eta_{complex}$ (blue value) has surpassed the other IQA methods, which identify the importance of k-space for MRI of healthy persons. Thus, K-CROSS still be able to serve as the metric for the synthesized quality of healthy person's neuroimage.

D. Segmentation Network Effect

Table V shows K-CROSS remains stable performance even using different state-of-the-art medical segmentation models.

TABLE IV

METRIC PERFORMANCE FOR HEALTHY PERSONS ON IXI. THE INCONSISTENCY IS COMPUTED, WHERE \downarrow IS BETTER. THE BEST RESULT IS IN RED AND THE SECOND BEST RESULT IS IN BLUE.

Metric	CycleGAN	MUNIT	UNIT
MAE [7]	0.3160	0.1809	0.2442
PSNR [15]	0.3388	0.1835	0.2419
SSIM [35]	0.3352	0.1962	0.2423
MS-SSIM [36]	0.3238	0.1945	0.2418
NLPD [19]	0.3135	0.1918	0.2409
GMSD [39]	0.3090	0.1908	0.2398
DeepIQA [4]	0.3043	0.1856	0.2381
LPIP [41]	0.3022	0.1810	0.2374
DIST [11]	0.3056	0.1805	0.2356
K-CROSS (\mathcal{L}_{stru})	0.3078	0.1790	0.2318
K-CROSS (\mathcal{L}_{comp})	0.3045	0.1618	0.2233
K-CROSS ($\mathcal{L}_{stru} + \mathcal{L}_{comp}$)	0.2876	0.1610	0.2150

Note that the parameters of the pre-trained segmentation network are frozen during the training phase. The first column denotes the segmentation method. We calculate the variance score of the K-CROSS value for CycleGAN, MUNIT and UNIT by using different segmentation backbone models. We find that the variance of K-CROSS performance is tiny (0.2%, 0.3%, and 0.2%). Hence, the performance of K-CROSS is not affected by the segmentation model.

TABLE V

THE EFFECT OF SEGMENTATION NETWORK FOR K-CROSS VALUE FOR VARIOUS GENERATIVE MODELS OF NIRPS.

Segmentation Model	CycleGAN	MUNIT	UNIT
nnUnet [16]	0.1872	0.2246	0.2160
AttnUnet [28]	0.1873	0.2268	0.2157
SETR [43]	0.1852	0.2254	0.2162
CoTr [37]	0.1856	0.2244	0.2154
TransUNet [9]	0.1862	0.2247	0.2162
SwinUNet [6]	0.1845	0.2252	0.2158

E. General Metric? Overcoming Domain Gap

The purpose of this paper is to demonstrate that K-CROSS is capable of serving as the standard measure for MRI datasets. We conduct extensive experiments and the results are given in Table VI, Table VII, and Table VIII to demonstrate that K-CROSS is not affected by dataset domain gap and the generative model. The training dataset is the BraTS dataset, and the test dataset is IXI. As described in Section V-C, we remove the tumor branch score, when K-CROSS evaluates the quality of neuroimage in healthy cases. We also observe that K-CROSS averagely surpasses DIST and LPIP (SOTA for natural image) by 7.8% and 16.5%, respectively, which proves that K-CROSS is built upon the basis of MRI principle instead of only on the natural image level. From this ablation study, we demonstrate that the performance of K-CROSS ($\mathcal{L}_{stru} + \mathcal{L}_{freq}$) is stable across several MRI datasets, with the potential to serve as a generic measure for evaluating the quality of the synthesized MRI.

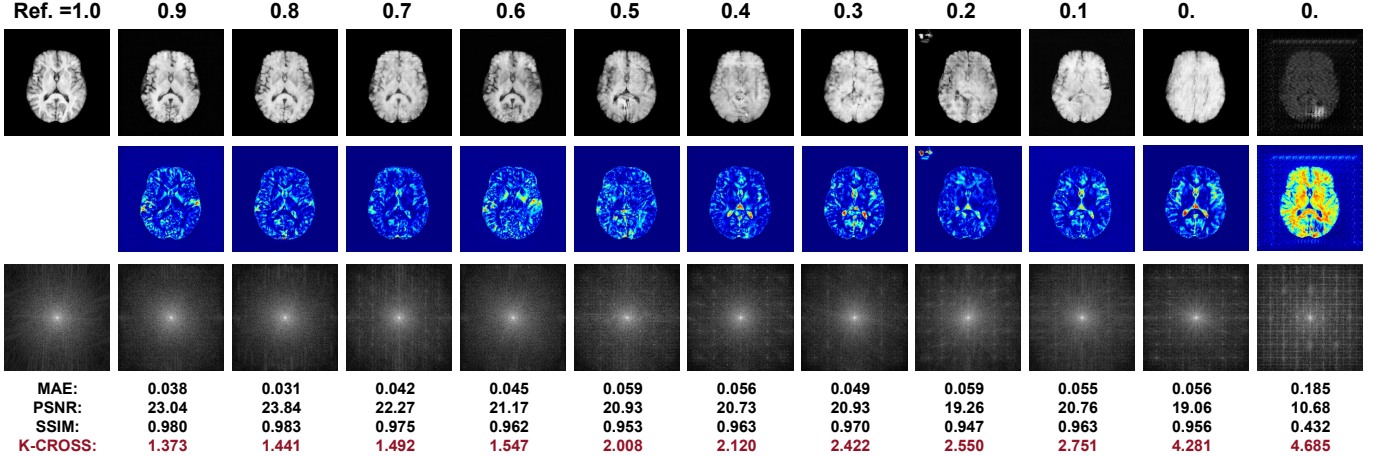


Fig. 10. Visualization of the NIRPS dataset. The number above each synthesized neuroimage is the radiologist's score. The blue map denotes the error map between the synthesis neuroimage data and the reference image. The third row represents the k-space map. A higher value of MAE, PSNR, SSIM and radiologist' score indicates higher performance of the synthesis quality. A lower value of K-CROSS indicates a higher performance of the synthesis quality. It's easily observed that K-CROSS is consistent with the order of the radiologist's score when the synthesis quality deteriorates but PSNR, SSIM and MAE are not.

TABLE VI
K-CROSS ON NIRPS (CYCLEGAN). THE INCONSISTENCY IS COMPUTED, WHERE \downarrow IS BETTER. THE BEST RESULT IS IN RED AND THE SECOND BEST RESULT IS IN BLUE.

Training Set (BraTS) Test Set (IXI)	T1-FLAIR PD-T2	T2-FLAIR PD-T2	T1-T2 PD-T2
MAE [7]	0.3208	0.3321	0.3228
PSNR [15]	0.3190	0.3270	0.3261
SSIM [35]	0.3231	0.3231	0.3212
MS-SSIM [36]	0.3189	0.3180	0.3128
NLPD [19]	0.3176	0.3163	0.3090
GMSD [39]	0.3067	0.3154	0.3067
DeepIQA [4]	0.3058	0.3124	0.3045
LPIP [41]	0.3033	0.3056	0.3039
DIST [11]	0.3021	0.3032	0.3006
K-CROSS (\mathcal{L}_{stru})	0.3018	0.3013	0.2990
K-CROSS (\mathcal{L}_{freq})	0.3015	0.2997	0.2953
K-CROSS ($\mathcal{L}_{stru} + \mathcal{L}_{freq}$)	0.2893	0.2950	0.2890

VI. CONCLUSION

In this paper, we proposed a new metric K-CROSS for assessing the performance of the synthesized medical images, which is built on the magnetic resonance imaging principle. To improve the capability of reconstruction during training K-CROSS, a complex U-Net was developed. As for training a learning-based full IQA metric, we further constructed a large-scale multi-modal neuroimaging perceptual similarity (NIRPS) dataset. Experimental results indicate that K-CROSS is a useful indicator for evaluating the quality of the generated medical data.

Limitation and Negative Society Impact Our method heavily relies on deep learning-based techniques but without directly injecting the knowledge of radiologists into K-CROSS. In the future, K-CROSS need to combine causal inference methods to enhance interpretability.

TABLE VII
K-CROSS ON THE NIRPS DATASET (MUNIT). THE INCONSISTENCY IS COMPUTED, WHERE \downarrow IS BETTER. THE BEST RESULT IS IN RED AND THE SECOND BEST RESULT IS IN BLUE.

Training Set Test Set	BraTS (T1-FLAIR) IXI (PD-T2)	BraTS (T2-FLAIR) IXI (PD-T2)	BraTS(T1-T2) IXI (PD-T2)
MAE [7]	0.1872	0.1865	0.1842
PSNR [15]	0.1853	0.1873	0.1853
SSIM [35]	0.1967	0.1986	0.1982
MS-SSIM [36]	0.1932	0.1952	0.1923
NLPD [19]	0.1945	0.1943	0.1921
GMSD [39]	0.1920	0.1934	0.1932
DeepIQA [4]	0.1835	0.1845	0.1856
LPIP [41]	0.1783	0.1754	0.1784
DIST [11]	0.1742	0.1731	0.1786
K-CROSS (\mathcal{L}_{stru})	0.1713	0.1720	0.1790
K-CROSS (\mathcal{L}_{freq})	0.1703	0.1709	0.1692
K-CROSS ($\mathcal{L}_{stru} + \mathcal{L}_{freq}$)	0.1688	0.1693	0.1617

TABLE VIII
K-CROSS ON THE NIRPS DATASET (UNIT). THE INCONSISTENCY IS COMPUTED, WHERE \downarrow IS BETTER. THE BEST RESULT IS IN RED AND THE SECOND BEST RESULT IS IN BLUE.

Training Set Test Set	BraTS (T1-FLAIR) IXI (PD-T2)	BraTS (T2-FLAIR) IXI (PD-T2)	BraTS (T1-T2) IXI (PD-T2)
MAE [7]	0.2468	0.2445	0.2480
PSNR [15]	0.2421	0.2410	0.2410
SSIM [35]	0.2545	0.2505	0.2470
MS-SSIM [36]	0.2486	0.2474	0.2463
NLPD [19]	0.2481	0.2461	0.2450
GMSD [39]	0.2410	0.2388	0.2478
DeepIQA [4]	0.2398	0.2376	0.2391
LPIP [41]	0.2352	0.2341	0.2384
DIST [11]	0.2348	0.2337	0.2386
K-CROSS (\mathcal{L}_{stru})	0.2323	0.2320	0.2250
K-CROSS (\mathcal{L}_{freq})	0.2190	0.2195	0.2250
K-CROSS ($\mathcal{L}_{stru} + \mathcal{L}_{freq}$)	0.2188	0.2188	0.2175

ACKNOWLEDGMENT

This work is partially supported by the National Key R&D Program of China (Grant NO. 2022YFF1202903) and the National Natural Science Foundation of China (Grant NO. 62122035, 61972188, and 62206122). Y. Jin is supported by

an Alexander von Humboldt Professorship for AI endowed by the German Federal Ministry of Education and Research.

REFERENCES

- [1] Abien Fred Agarap. Deep learning using rectified linear units (relu). *ArXiv*, abs/1803.08375, 2018. [3](#)
- [2] Paul Aljabar, Robin Wolz, Latha Srinivasan, Serena J. Counsell, Mary A. Rutherford, Anthony David Edwards, Joseph V. Hajnal, and Daniel Rueckert. A combined manifold learning analysis of shape and appearance to characterize neonatal brain development. *IEEE Transactions on Medical Imaging*, 30:2072–2086, 2011. [6](#)
- [3] Spyridon Bakas, Hugo J. Kuijf, Bjoern H. Menze, and Mauricio Reyes. Brainlesion: Glioma, multiple sclerosis, stroke and traumatic brain injuries. In *Lecture Notes in Computer Science*, 2017. [6](#)
- [4] Sebastian Bosse, Dominique Maniry, Klaus-Robert Müller, Thomas Wiegand, and Wojciech Samek. Deep neural networks for no-reference and full-reference image quality assessment. *IEEE Transactions on Image Processing*, 27:206–219, 2018. [7](#), [8](#), [9](#)
- [5] Sebastian Bosse, Dominique Maniry, Thomas Wiegand, and Wojciech Samek. A deep neural network for image quality assessment. *2016 IEEE International Conference on Image Processing (ICIP)*, pages 3773–3777, 2016. [2](#)
- [6] Hu Cao, Yueyue Wang, Joy Chen, Dongsheng Jiang, Xiaopeng Zhang, Qi Tian, and Manning Wang. Swin-unet: Unet-like pure transformer for medical image segmentation. *ArXiv*, abs/2105.05537, 2021. [3](#), [8](#)
- [7] Tianfeng Chai and Roland R. Draxler. Root mean square error (rmse) or mean absolute error (mae)? – arguments against avoiding rmse in the literature. *Geoscientific Model Development*, 7:1247–1250, 2014. [1](#), [7](#), [8](#), [9](#)
- [8] Tong Che, Yanran Li, Athul Paul Jacob, Yoshua Bengio, and Wenjie Li. Mode regularized generative adversarial networks. *ArXiv*, abs/1612.02136, 2017. [2](#)
- [9] Jieneng Chen, Yongyi Lu, Qihang Yu, Xiangde Luo, Ehsan Adeli, Yan Wang, Le Lu, Alan Loddon Yuille, and Yuyin Zhou. Transunet: Transformers make strong encoders for medical image segmentation. *ArXiv*, abs/2102.04306, 2021. [3](#), [8](#)
- [10] Michael Cogswell, Faruk Ahmed, Ross B. Girshick, C. Lawrence Zitnick, and Dhruv Batra. Reducing overfitting in deep networks by decorrelating representations. *CoRR*, abs/1511.06068, 2016. [4](#)
- [11] Keyan Ding, Kede Ma, Shiqi Wang, and Eero P. Simoncelli. Image quality assessment: Unifying structure and texture similarity. *IEEE Transactions on Pattern Analysis and Machine Intelligence*, 44:2567–2581, 2022. [7](#), [8](#), [9](#)
- [12] Arthur Gretton, Bharath K. Sriperumbudur, D. Sejdinovic, Heiko Strathmann, Sivaraman Balakrishnan, Massimiliano Pontil, and Kenji Fukumizu. Optimal kernel choice for large-scale two-sample tests. In *NIPS*, 2012. [2](#)
- [13] Martin Heusel, Hubert Ramsauer, Thomas Unterthiner, Bernhard Nessler, and Sepp Hochreiter. Gans trained by a two time-scale update rule converge to a local nash equilibrium. In *NIPS*, 2017. [2](#)
- [14] Xun Huang, Ming-Yu Liu, Serge Belongie, and Jan Kautz. Multimodal unsupervised image-to-image translation. In *Proceedings of the European conference on computer vision (ECCV)*, pages 172–189, 2018. [6](#)
- [15] Quan Huynh-Thu and Mohammed Ghanbari. Scope of validity of psnr in image/video quality assessment. *Electronics Letters*, 44:800–801, 2008. [1](#), [7](#), [8](#), [9](#)
- [16] Fabian Isensee, Paul F. Jaeger, Simon A. A. Kohl, Jens Petersen, and Klaus Maier-Hein. nnu-net: a self-configuring method for deep learning-based biomedical image segmentation. *Nature methods*, 2020. [3](#), [4](#), [8](#)
- [17] Liming Jiang, Bo Dai, Wayne Wu, and Chen Change Loy. Focal frequency loss for image reconstruction and synthesis. *2021 IEEE/CVF International Conference on Computer Vision (ICCV)*, pages 13899–13909, 2021. [5](#)
- [18] B.L. Kalman and S.C. Kwasny. Why tanh: choosing a sigmoidal function. In *[Proceedings 1992] IJCNN International Joint Conference on Neural Networks*, volume 4, pages 578–581 vol.4, 1992. [4](#)
- [19] Valero Laparra, Johannes Ballé, Alexander Berardino, and Eero P. Simoncelli. Perceptual image quality assessment using a normalized laplacian pyramid. In *HVEI*, 2016. [7](#), [8](#), [9](#)
- [20] Kwan-Yee Lin and Guanxiang Wang. Hallucinated-iqa: No-reference image quality assessment via adversarial learning. *2018 IEEE/CVF Conference on Computer Vision and Pattern Recognition*, pages 732–741, 2018. [2](#)
- [21] Ming-Yu Liu, Thomas M. Breuel, and Jan Kautz. Unsupervised image-to-image translation networks. In *NIPS*, pages 700–708, 2017. [6](#)
- [22] Xialei Liu, Joost van de Weijer, and Andrew D. Bagdanov. Rankiqa: Learning from rankings for no-reference image quality assessment. *2017 IEEE International Conference on Computer Vision (ICCV)*, pages 1040–1049, 2017. [2](#)
- [23] Andrew L. Maas. Rectifier nonlinearities improve neural network acoustic models. 2013. [3](#)
- [24] Anish Mittal, Rajiv Soundararajan, and Alan Conrad Bovik. Making a “completely blind” image quality analyzer. *IEEE Signal Processing Letters*, 20:209–212, 2013. [2](#)
- [25] Anush K. Moorthy and Alan Conrad Bovik. Blind image quality assessment: From natural scene statistics to perceptual quality. *IEEE Transactions on Image Processing*, 20:3350–3364, 2011. [2](#)
- [26] Hongyu Ren, Diqi Chen, and Yizhou Wang. Ran4iqa: Restorative adversarial nets for no-reference image quality assessment. In *AAAI*, 2018. [2](#)
- [27] Tim Salimans, Ian J. Goodfellow, Wojciech Zaremba, Vicki Cheung, Alec Radford, and Xi Chen. Improved techniques for training gans. In *NIPS*, 2016. [2](#)
- [28] Jo Schlemper, Ozan Oktay, Michiel Schaap, Matthias P. Heinrich, Bernhard Kainz, Ben Glocker, and Daniel Rueckert. Attention gated networks: Learning to leverage salient regions in medical images. *Medical image analysis*, 53:197 – 207, 2019. [8](#)
- [29] Rebecca L. Siegel, Kimberly D Miller, and Ahmedin Jemal. Cancer statistics, 2019. *CA: A Cancer Journal for Clinicians*, 69, 2019. [6](#)
- [30] Karen Simonyan and Andrew Zisserman. Very deep convolutional networks for large-scale image recognition. *CoRR*, abs/1409.1556, 2015. [5](#)
- [31] Christian Szegedy, Vincent Vanhoucke, Sergey Ioffe, Jonathon Shlens, and Zbigniew Wojna. Rethinking the inception architecture for computer vision. *2016 IEEE Conference on Computer Vision and Pattern Recognition (CVPR)*, pages 2818–2826, 2016. [2](#)
- [32] Heountaek Lim, Hak Gu Kim, and Yong Man Ro. Vr iqa net: Deep virtual reality image quality assessment using adversarial learning. *2018 IEEE International Conference on Acoustics, Speech and Signal Processing (ICASSP)*, pages 6737–6741, 2018. [2](#)
- [33] Hossein Talebi and Peyman Milanfar. Nima: Neural image assessment. *IEEE Transactions on Image Processing*, 27:3998–4011, 2018. [2](#)
- [34] Chiheb Trabelsi, Oleksa Bilaniuk, Dmitriy Serdyuk, Sandeep Subramanian, João Felipe Santos, Soroush Mehri, Negar Rostamzadeh, Yoshua Bengio, and Christopher Joseph Pal. Deep complex networks. *ArXiv*, abs/1705.09792, 2018. [3](#)
- [35] Zhou Wang, Alan Conrad Bovik, Hamid R. Sheikh, and Eero P. Simoncelli. Image quality assessment: from error visibility to structural similarity. *IEEE Transactions on Image Processing*, 13:600–612, 2004. [1](#), [2](#), [7](#), [8](#), [9](#)
- [36] Zhou Wang, Eero P. Simoncelli, and Alan Conrad Bovik. Multi-scale structural similarity for image quality assessment. 2003. [2](#), [7](#), [8](#), [9](#)
- [37] Yutong Xie, Jianpeng Zhang, Chunhua Shen, and Yong Xia. Cotr: Efficiently bridging cnn and transformer for 3d medical image segmentation. In *MICCAI*, 2021. [8](#)
- [38] Qiantong Xu, Gao Huang, Yang Yuan, Chuan Guo, Yu Sun, Felix Wu, and Kilian Q. Weinberger. An empirical study on evaluation metrics of generative adversarial networks. *ArXiv*, abs/1806.07755, 2018. [2](#)
- [39] Wufeng Xue, Lei Zhang, Xuanqin Mou, and Alan Conrad Bovik. Gradient magnitude similarity deviation: A highly efficient perceptual image quality index. *IEEE Transactions on Image Processing*, 23:684–695, 2014. [7](#), [8](#), [9](#)
- [40] Lin Zhang, Lei Zhang, Xuanqin Mou, and David Zhang. Fsim: A feature similarity index for image quality assessment. *IEEE Transactions on Image Processing*, 20:2378–2386, 2011. [2](#)
- [41] Richard Zhang, Phillip Isola, Alexei A. Efros, Eli Shechtman, and Oliver Wang. The unreasonable effectiveness of deep features as a perceptual metric. *2018 IEEE/CVF Conference on Computer Vision and Pattern Recognition*, pages 586–595, 2018. [2](#), [5](#), [7](#), [8](#), [9](#)
- [42] Weixia Zhang, Kede Ma, Guangtao Zhai, and Xiaokang Yang. Uncertainty-aware blind image quality assessment in the laboratory and wild. *IEEE Transactions on Image Processing*, 30:3474–3486, 2021. [2](#)
- [43] Sixiao Zheng, Jiachen Lu, Hengshuang Zhao, Xiatian Zhu, Zekun Luo, Yabiao Wang, Yanwei Fu, Jianfeng Feng, Tao Xiang, Philip H. S. Torr, and Li Zhang. Rethinking semantic segmentation from a sequence-to-sequence perspective with transformers. *2021 IEEE/CVF Conference on Computer Vision and Pattern Recognition (CVPR)*, pages 6877–6886, 2021. [8](#)
- [44] Jun-Yan Zhu, Taesung Park, Phillip Isola, and Alexei A Efros. Unpaired image-to-image translation using cycle-consistent adversarial networks. In *Proceedings of the IEEE international conference on computer vision*, pages 2223–2232, 2017. [6](#)